Demonstration of Real-Time Software Reconfigurable Dynamic Power-and-Subcarrier Allocation Scheme for OFDM-NOMA-Based Multi-User Visible Light Communications

Jin Shi, Yang Hong, *Member, IEEE*, Rui Deng, Jing He, Lian-Kuan Chen, *Senior Member, IEEE*, and Gee-Kung Chang, *Fellow, IEEE, Fellow, OSA*

***Abstract*—We propose and demonstrate a real-time software reconfigurable dynamic power-and-subcarrier allocation scheme for orthogonal frequency division multiplexing based non-orthogonal multiple access (OFDM-NOMA) in visible light communications (VLC) systems. The key digital signal processing algorithms for real-time OFDM-NOMA implementations are illustrated in details. With the help of the software reconfigurable technique, the power ratios of different sub-bands can be dynamically adjusted according to the channel conditions, resulting in superior user fairness and optimal transmission performance. Moreover, the subcarrier number of each user can also be flexibly controlled to fulfill the corresponding capacity demands. To validate the effectiveness of the proposed scheme, we consider different user scenarios with various path losses for extensive performance evaluations. Experimental results show that 1.84-Gbit/s real-time OFDM-NOMA transmission can achieve stable operation over several hours, wherein the BER is below the hard-decision forward error correction threshold of 3.8×10^{-3}. The proposed scheme provides a promising solution for practical implementations of multi-user VLC, as it is markedly adaptive to dynamic capacity demands while maintaining better user fairness and system flexibility and stability.**

***Index Terms*—Non-orthogonal multiple access (NOMA), OFDM, real-time FPGA, visible light communications (VLC).**

Manuscript received April 11, 2019; revised June 12, 2019; accepted June 20, 2019. Date of publication June 26, 2019; date of current version August 22, 2019. This work was supported in part by the National Natural Science Foundation of China under Grant 61775054, in part by the Science and Technology Project of Hunan Province under Grant 2016GK2011, and in part by the HKSAR RGC grant (GRF 14201217). *(Corresponding author: Jing He.)*

J. Shi and J. He are with the College of Computer Science and Electronic Engineering, Hunan University, Changsha 410082, China (e-mail: jhe@hnu.edu.cn).

Y. Hong was with the Department of Information Engineering, The Chinese University of Hong Kong. He is now with the Optoelectronics Research Centre, University of Southampton, Southampton SO17 1BJ, U.K. (e-mail: y.hong@soton.ac.uk).

R. Deng and L.-K. Chen are with the Department of Information Engineering, The Chinese University of Hong Kong, Hong Kong SAR (e-mail: rdeng@ie.cuhk.edu.hk; lkchen@ie.cuhk.edu.hk).

G.-K. Chang is with the School of Electrical and Computer Engineering, Georgia Institute of Technology, Atlanta, GA 30308 USA (e-mail: geekung.chang@ece.gatech.edu).

Color versions of one or more of the figures in this paper are available online at http://ieeexplore.ieee.org.

Digital Object Identifier 10.1109/JLT.2019.2924935

I. Introduction

VISIBLE light communication (VLC) has been recognized as a promising technology for future optical wireless communication due to its advantages such as immunity to electromagnetic interference, low power consumption, simple installation, and license-free spectrum availability [1], [2]. While most of the prior works explore the maximization of system capacity by using advanced digital signal processing (DSP) for point-to-point transmissions [3]–[5], the multiple access (MA) technologies also play important roles in VLC, as it is essential to provide simultaneous multi-user services. Conventional MA technologies, such as frequency division multiple access (FDMA), time division multiple access (TDMA), code division multiple access (CDMA), and orthogonal frequency division multiplexing access (OFDMA), have been reported to improve VLC system performance [6], [7]. In order to satisfy the increasing demands in mobile data traffic, high spectral efficiency and massive connectivity are required. However, conventional MA technologies require strict orthogonality in time, frequency or code domain in order to avoid multi-user interference, which severely limits the number of supported users. Recently, power domain non-orthogonal multiple access (NOMA) has been gaining tremendous interests from both industry and academia [8]. It has been demonstrated that NOMA can achieve improved spectral efficiency and allow more connectivity compared to OFDM. In a NOMA based system, multiple users sharing the same time and frequency resources are capable of transmitting signals configured with different power weights, leading to better user fairness and enhanced system throughput. NOMA has been experimentally demonstrated in optical communications including both radio-over-fiber (RoF) systems and VLC systems [9]–[12]. In [9], OFDM-NOMA is applied in a 60-GHz-millimeter-wave RoF system, which significantly improves reception quality and system reliability due to the utilization of power allocation between different users. In [10], the combination of NOMA and multiband carrierless amplitude phase modulation (multiCAP) is experimentally demonstrated for RoF in the W-band, allowing the optimization of available capacity as well as flexible user provisioning. For VLC scenarios, bidirectional OFDM-NOMA has been demonstrated in a VLC system, which exhibits a higher

capacity for supporting more users [13]. In [14], a phase predistortion method is proposed and experimentally demonstrated to solve the phase mismatch in uplink OFDM-NOMA VLC system. In [15], offset quadrature amplitude modulation (OQAM)-OFDM based NOMA is proposed and demonstrated in multiple-input and multiple-output (MIMO) VLC system, wherein higher spectral efficiency and an aggregate capacity of 3.2 gigabit-per-second (Gbit/s) are realized.

However, most of these results are based on offline experiments without the considerations of practical real-time implementations. For practical implementations, dynamic and diverse channel conditions will affect the flexibility and robustness of these systems, as static parameter setting is assumed in the offline experiments [16]. Moreover, subcarrier allocation, which has not been considered, is also crucial to optimize the system performance especially when different power fading conditions over subcarriers/users are experienced in the bandwidth-limited VLC system. Therefore, it is highly desirable that the software-configurable control can be supported in a real-time manner to dynamically handle parameters such as power ratio and subcarrier number so as to realize flexible capacity control and to implement resource allocations according to users' demands in OFDM-NOMA based VLC systems.

In this paper, we extend our preliminary work in [17], with detailed principles of operation and extensive experimental investigations presented in real-time OFDM-NOMA based multi-user VLC systems. The digital signal processing (DSP) functions at both transmitter and receiver are fully performed using Xilinix-7 field programmable gate array (FPGA) to realize real-time transmissions. Zero-tailed based direct-current-biased optical OFDM (DCO-OFDM) is proposed for the real-time transmitter to reduce the implementation complexity. Meanwhile, at the receiver, the demodulation of OFDM-NOMA is redesigned and overhauled so as to facilitate the hardware implementation in real-time. Furthermore, in order to optimize the system performance, the power ratio is investigated in multi-band OFDM-NOMA to mitigate the severe high-frequency fading induced performance degradation. In addition, the system can support software-configuration for dynamic power-and-subcarrier allocation in real-time, exhibiting higher flexibility and better adaption to user demands. It is demonstrated that when varying the channel conditions, the power ratio can be dynamically adjusted, so as to achieve better user fairness as well as optimal system performance. Meanwhile, the data rate can be flexibly controlled to fulfill the capacity demands of each user.

II. The Operation Principle of OFDM-NOMA

A. Zero-Tailed Based DCO-OFDM in VLC System

In VLC systems, real-valued time domain signals should be generated due to the advantages of intensity modulation (IM) [18], [19]. Thus, DCO-OFDM transmitter is a straightforward option for deploying such systems. It involves the addition of direct-current (DC) bias to the bipolar signal, making it unipolar [19]. Fig. 1(a) illustrates the conventional DCO-OFDM transmitters based on Hermitian symmetry (HS) [20], [21]. The complex data vector, $\mathbf{X} = [X(0),\ X(1),\ X(2), \ldots$

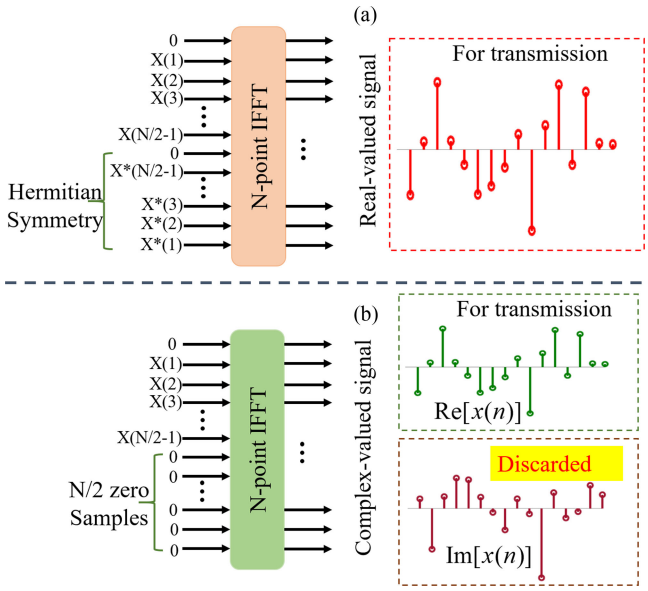

Fig. 1. Two types of DCO-OFDM transmitters based on (a) Hermitian symmetry and (b) Zero-tailed. Note that the only difference between HS-based DCO-OFDM and the Zero-tailed DCO-OFDM is that the amplitude of the Zero-tailed scheme is halved.

$X(N-1)]$, is the original data after quadrature amplitude modulation (QAM) mapping. For most of DCO-OFDM systems, Hermitian symmetry operation, namely, $X(N-k) = X^*(k),\ k = 1,\ 2,\ \ldots N-1;\ X(0) = X(N/2) = 0,$ is imposed in the frequency domain to obtain real-valued OFDM signals [18], as shown in Fig. 1(a). The time-domain OFDM signal after inverse fast Fourier transform (IFFT) is given by [22]

$$x(n) = \frac{1}{N}\sum_{k=0}^{N-1} X(k)\exp\left(\frac{j2\pi kn}{N}\right),\ n = 0,\ 1,\ \ldots,\ N-1 \tag{1}$$

When implementing the HS-based real-valued OFDM using the FPGA, a number of register resources are required to restore and calculate the Hermitian symmetric data. This gives rise to redundancy/delay as IFFT can only be performed until all input data is available. To avoid this issue, in this work, a low-complexity scheme, termed Zero-tailed based DCO-OFDM, is proposed to generate the real-valued OFDM signal. As shown in Fig. 1(b), the QAM-mapped complex data is arranged as $\mathbf{X} = [0, X_1, X_2 \ldots X(N/2-1),\ \underbrace{0, 0, \ldots 0}_{N/2}]$, where N/2 zero samples are inserted in the second half of data subcarriers. After N-point IFFT, the time-domain OFDM signal with complex-valued is attained. It can be found that the real part of obtained complex signal is the same as the real-valued signal obtained by HS-based DCO-OFDM, except that the amplitude is halved. Therefore, for Zero-tailed DCO-OFDM, the imaginary parts are discarded, and only the real parts of complex signal are used for transmission, as marked in Fig. 1(b). It is worth noting that the idea of the Zero-tailed DCO-OFDM is to reduce the

HS-induced computation and redundancy/delay in FPGA-based real-time implementations. Since it will not change the time-domain waveform of the generated OFDM signal (except that the amplitude is halved), the corresponding DSP at the receiver is also identical for the zero-tailed DCO-OFDM and HS-based DCO-OFDM. Thus, they can achieve identical performance. As for the asymmetrically clipped optical OFDM (ACO-OFDM), its spectral efficiency is halved compared to that of the DCO-OFDM in order to directly generate unipolar time-domain waveforms. Moreover, it also requires extra digital clipping operation as its peak-to-average power ratio (PAPR) is higher than DCO-OFDM. Therefore, to maximize the spectral efficiency whilst minimize the implementation complexity of the real-time VLC system, the zero-tailed DCO-OFDM scheme is adopted in this work.

B. Non-Orthogonal Multiple Access (NOMA)

NOMA, as a promising MA technique, can multiplex multiple users in the power domain while sharing the same time-frequency resources [23]. Moreover, it is fully compatible with existing time or frequency multiplexing schemes [9]–[12]. In practical applications, certain users, especially those located at the edge of cells, will suffer severe path losses, resulting in low signal-to-noise ratio (SNR) conditions. In contrast, users located at the central area of cells will exhibit higher SNR due to higher received signal power. As a result, there exists some disparities in SNR conditions due to different path losses among different users. The users with high SNR have extra margins of power budget while the users with low SNR require more power to enhance the performance. In such cases, NOMA can be used to achieve better performance and user fairness thanks to the adoption of power allocation. Assuming there are two users with different channel conditions, after overlapping in the power domain with different power weights, the generated NOMA signal in the frequency domain is given by [15]

$$X_{NOMA} = \sqrt{P_1}X_1 + \sqrt{P_2}X_2 \tag{2}$$

where X_1 denotes the signal of UE1 with an inferior channel condition, requiring a high power P_1. X_2 is the signal of UE2 with a good channel condition and thus requires a low power P_2. In order to recover users' information at the receiver, UE1 is directly de-modulated from the overlapped signal by treating UE2 as the noise. For the demodulation of UE2, the successive interference cancellation (SIC) algorithm is used to eliminate the multi-user interference by subtracting the signal component of UE1 from the received overlapped signal [9]. Subsequently, the desired signal UE2 can be decoded correctly.

III. Real-Time DSP Algorithm of OFDM-NOMA

In this section, we describe several key real-time DSP algorithms for the FPGA implementation of OFDM-NOMA, including the data frame structure, channel estimation and equalization, and multi-user demodulation with a simplified SIC algorithm.

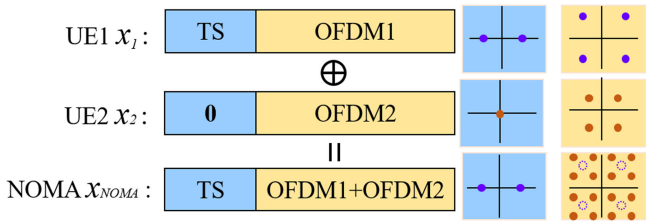

Fig. 2. Data frame structure of real-time OFDM-NOMA at transmitter.

A. Data Frame Structure at Transmitter

Fig. 2 shows the data frame structure of real-time OFDM-NOMA at transmitter. The data frame for UE1 consists of a training sequence (TS) and OFDM symbols. The TS designed here is used for channel estimation. The beginning of the data frame for UE2 is filled with the same length of zeros. After the overlapping of both users' data with different power weights, the resulting NOMA signal will be transmitted and detected at receivers of UE1 and UE2, wherein the corresponding propagation paths are different. Note that the TS in UE1 can also be used to estimate the channel response at the receiver of UE2.

B. Channel Estimation and Equalization

At the receiver, an effective synchronization scheme, as described in [24], is first performed to find the beginning in the received data frame. Then, the channel response is estimated for subsequent signal equalization. It is worth noting that, in this paper, the channel estimation is used not only for equalization, but also for performing the SIC algorithm, which will be explained in the following. In order to reduce the complexity, the channel estimation is specially designed. At the transmitter, the training sequence (TS) is composed of binary phase shift keying (BPSK) symbols ([1 or -1]). It can greatly reduce the computational complexity for channel estimation because it does not require the complex division operations and only needs to change the signs of received TS accordingly. The estimated channel response is [24], [25]

$$\hat{H}(k) = \frac{TS_{rv}(k)}{TS_{local}(k)} = sign[TS_{local}(k)] \times TS_{rv}(k) \tag{3}$$

where $TS_{rv}(k)$ and $TS_{local}(k)$ are the *k-th* subcarrier component of received TS and the pre-known TS, respectively. $sign[\bullet]$ is used to extract the sign of a real component. The estimated channel response, containing both amplitude and phase responses, will then be used to compensate the amplitude and phase distortions induced by the overall electrical-optical-electrical conversions. The equalized signal can be expressed as

$$\begin{aligned}\hat{R}_{rv}(k) &= \frac{R_{rv}(k)}{\hat{H}(k)} = \frac{R_{rv}(k)\hat{H}^*(k)}{|\hat{H}(k)|^2} \\ &= \frac{sign[TS_{local}(k)] \times R_{rv}(k) \times TS^*_{rv}(k)}{|TS_{rv}(k)|^2}\end{aligned} \tag{4}$$

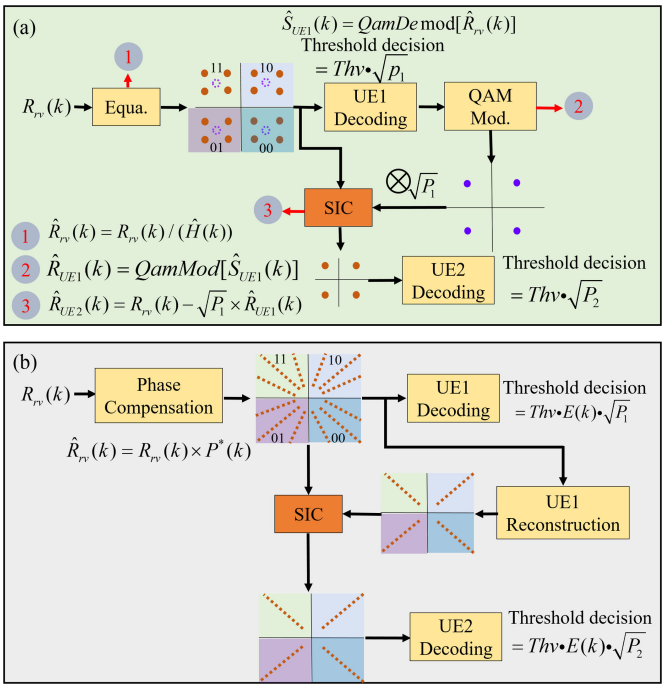

Fig. 3. Flow chart of multi-user interference cancellation process based on (a) offline realization and (b) proposed real-time implementation.

where $\hat{R}_{rv}(k)$ and $R_{rv}(k)$ are the received signal after and before both amplitude and phase equalization, respectively. Note that in order to avoid using the complex division shown in (4), only phase compensation is carried out in the channel equalization, namely, only the numerator part in (4) is executed in the equalization stage. As for the denominator part that is related to amplitude compensation, it will be considered in the de-mapping stage by altering the corresponding decision thresholds as described in the following sub-section.

C. Multiple Users Demodulation Based on Offline and Real-Time Realizations

Fig. 3 illustrates the processing diagrams of MUI cancellation based on (a) conventional offline realization and (b) proposed real-time implementation, respectively. As shown in Fig. 3(a), the offline processing algorithm can be summarized as follows. Firstly, the received signal is equalized using the estimated channel response as

$$\hat{R}_{rv}(k) = R_{rv}(k)/\hat{H}(k) \tag{5}$$

Secondly, the signal of UE1 can be directly decoded from the equalized signal and the decision threshold is redesigned as

$$\hat{S}_{UE1}(k) = \text{QamDemod}\left(\hat{R}_{rv}(k)\right),\ \text{Threshold} : Thv \bullet \sqrt{P_1} \tag{6}$$

where QamDemod(•) is the function of QAM de-mapper. The decision threshold for original QAM symbol is defined as *Thv*.

The threshold for UE1 is rescaled to $Thv \bullet \sqrt{P_1}$ due to the corresponding power allocation. Thirdly, in order to extract the UE2 from the overlapped signal, the signal of UE1, which is treated as interference in the demodulation of UE2, should be removed. Thus, the signal of UE1 is re-modulated and then removed, which is given by

$$\begin{aligned} \hat{R}_{UE1}(k) &= \text{QamMod}\left(\hat{S}_{UE1}(k)\right) \\ \hat{R}_{UE2}(k) &= R_{rv}(k) - \sqrt{P_1} \times \hat{R}_{UE1}(k) \end{aligned} \tag{7}$$

where QamMod(•) represents the function of QAM mapper. Finally, the signal of UE2 can be decoded and the decision threshold is given as

$$\begin{aligned} \hat{S}_{UE2}(k) &= \text{QamDemod}\left(\hat{R}_{UE2}(k)\right), \\ \text{Threshold} &: Thv \bullet \sqrt{P_2} \end{aligned} \tag{8}$$

In contrast, Fig. 3(b) illustrates the flow chart of proposed real-time MUI cancellation algorithm. Firstly, according to (4), we can formulate the phase compensation factor *P*(*k*) and amplitude compensation factor *E*(*k*) as

$$\begin{cases} P(k) = sign[TS_{local}(k)] \times TS^*_{rv}(k) \\ E(k) = |TS_{rv}(k)|^2 \end{cases} \tag{9}$$

Then, the phase compensation is performed as

$$\hat{R}_{rv}(k) = R_{rv}(k) \times P(k) \tag{10}$$

Since the amplitude response of the channel is not flat due to the high-frequency fading, the amplitude of the equalized constellation is also not uniform. Therefore, the decision thresholds are different for subcarriers, and they can be obtained by $Thv \bullet E(k) \bullet \sqrt{P_1}$. Based on the decision thresholds, the signal of UE1 can be decoded as

$$\begin{aligned} \hat{S}_{UE1}(k) &= \text{QamDemod}\left(\hat{R}_{rv}(k)\right) \\ \text{Threshold} &: Thv \bullet E(k) \bullet \sqrt{P_1} \end{aligned} \tag{11}$$

Notably, for each user with QPSK modulation, the value of decision threshold *Thv* is zero. Thus, the decision threshold for UE1 demodulation can be simplified as

$$\text{Threshold}: \ Thv \bullet E(k) \bullet \sqrt{P_1} = 0 \tag{12}$$

As aforementioned, to decode the signal of UE2, the signal of UE1 should be first re-modulated and then removed from the overlapped signal. Taking the amplitude compensation factor into account, the signal reconstruction of UE1 is performed as

$$\begin{cases} \Re\left(\hat{R}_{UE1}(k)\right) = \begin{cases} E(k) & \Re(\hat{R}_{rv}(k)) \geq 0 \\ -E(k) & \Re(\hat{R}_{rv}(k)) < 0 \end{cases} \\ \Im\left(\hat{R}_{UE1}(k)\right) = \begin{cases} E(k) & \Im(\hat{R}_{rv}(k)) \geq 0 \\ -E(k) & \Im(\hat{R}_{rv}(k)) < 0 \end{cases} \end{cases} \tag{13}$$

where $\Re(\bullet)$ and $\Im(\bullet)$ stand for the real and imaginary part of a complex component, respectively. The signal of UE2 can then be obtained as

$$\hat{R}_{UE2}(k) = R_{rv}(k) - \hat{R}_{UE1}(k) \tag{14}$$

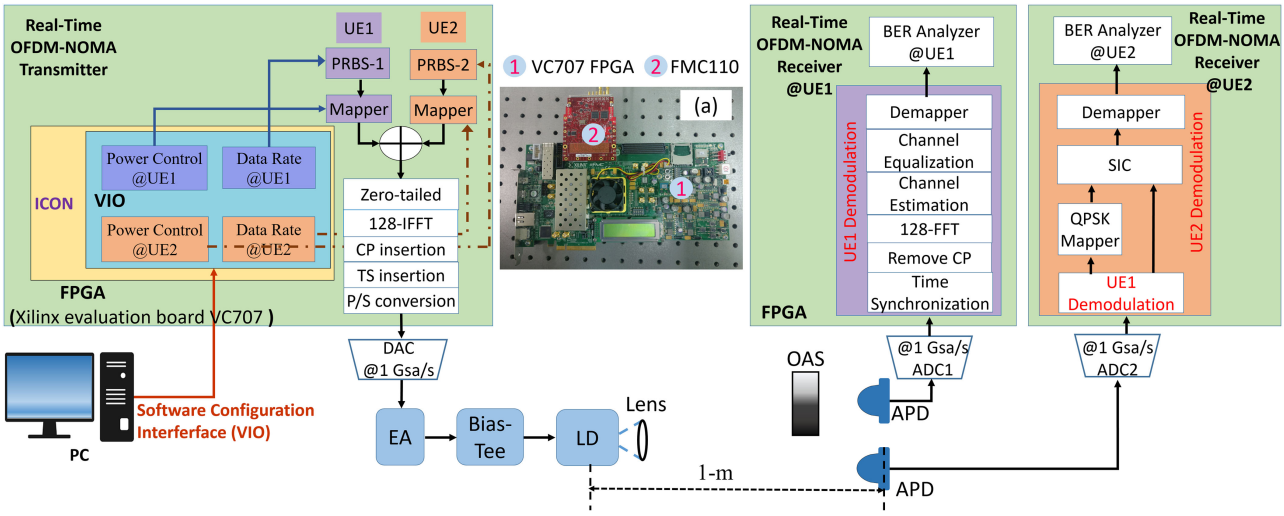

Fig. 4. Diagram of the real-time OFDM-NOMA VLC system. Inset (a) shows the FPGA board and the DAC/ADC card used for experiment.

Finally, the signal of UE2 can be decoded as

$$\hat{S}_{UE2}(k) = \text{QamDemod}\left(\hat{R}_{UE2}(k)\right) \quad \text{Threshold}: \ 0, \ \text{For QPSK Modulation} \tag{15}$$

IV. Real-Time Experimental Setup

The experimental setup of the real-time software-reconfigurable OFDM-NOMA based VLC system is shown in Fig. 4. Although the transmission distance is fixed to 1 meter in the setup, as will be investigated later, a variable optical attenuation slice (OAS) will be used to vary the received power at the avalanche photo diode (APD) so as to emulate the scenarios wherein longer distances are explored. The OFDM-NOMA transmitter and receiver are implemented in real-time by using a Xilinx evaluation board (VC707) and a 4DSP daughter card (FMC110) which provides dual-channel analog-to-digital converter (ADC) and dual-channel digital-to-analog converter (DAC). At the transmitter, two original binary data streams are generated by two pseudo-random binary sequence generators (PRBS). Then, the generated sequences are mapped into QPSK symbol sequences for UE1 and UE2, respectively. The power weighting factors of UE1 and UE2 can be dynamically controlled by a virtual input/output (VIO) intellectual property core [26], leading to the software-reconfigurable power allocation capability. Moreover, the numbers of effective data subcarriers of UE1 and UE2 can also be adjusted by VIO in real-time. After symbol overlapping in the frequency domain, zero-tailed operation for intensity modulation is performed before IFFT processing, which has a block size of 128. Note that except the DC subcarrier (index is 0), the 1-st, 62-nd and 63-rd subcarriers are also set as zero to minimize the DC blocking induced fading at low frequencies and bandwidth limitation induced fading at high frequencies. Thus, the available number of data subcarriers is 60. After 128-point IFFT, only the real parts of obtained complex signals are used for further transmission and the imaginary parts are discarded. Then, an 8-sample cyclic prefix (CP) is appended to the beginning of the every OFDM-NOMA symbol to avoid inter-symbol interference (ISI). Subsequently, two TS symbols for synchronization and channel estimation are inserted at the beginning of every OFDM-NOMA frame. Note that to minimize the complexity of the real-time VLC system, the generated OFDM signals were directly fed to the DAC without using clipping or other PAPR reduction techniques. After parallel-to-serial (P/S) conversion, the digital OFDM-NOMA signal is converted into an analog signal by a 12-bit 1-GSa/s DAC. In this paper, eight parallel data streams per FPGA clock cycle are utilized to realize high-speed transmission. The output of the DAC is amplified by an electrical amplifier (EA). The amplified signal, together with a DC bias, is then used to drive a blue laser diode (LD, Osram PL450). In front of the LD, a bi-convex lens is used to collimate the light.

After 1-m free space transmission, two identical APDs are used for signal detection for UE1 and UE2, respectively. An OAS is placed in front of the APD of UE1 to attenuate the received light, so as to emulate an inferior channel condition. At the receiver of UE1, the detected electrical signal by the APD is then converted into digital signal by an ADC with a 1-GSa/s sampling rate. Fig. 4 also shows the detailed DSP blocks at the receiver of UE1, which include symbol synchronization, CP removal, 128-point FFT, channel estimation and equalization, de-mapper, and error counting. As aforementioned, for demodulation of UE1, the interference from UE2 is treated as noise due to its small power allocation. At the receiver of UE2, UE1's demodulation is firstly carried out, and then SIC algorithm is utilized to remove the interference from the UE1 so as to recover the signal of UE2.

V. Real-Time Experimental Results and Discussion

A. Soft-Reconfigurable Platform for OFDM-NOMA

Fig. 5 shows the real-time control interface based on Chipscope. Both power allocation and subcarrier number can be flexibly controlled according to user demands as shown in Fig. 5(a).

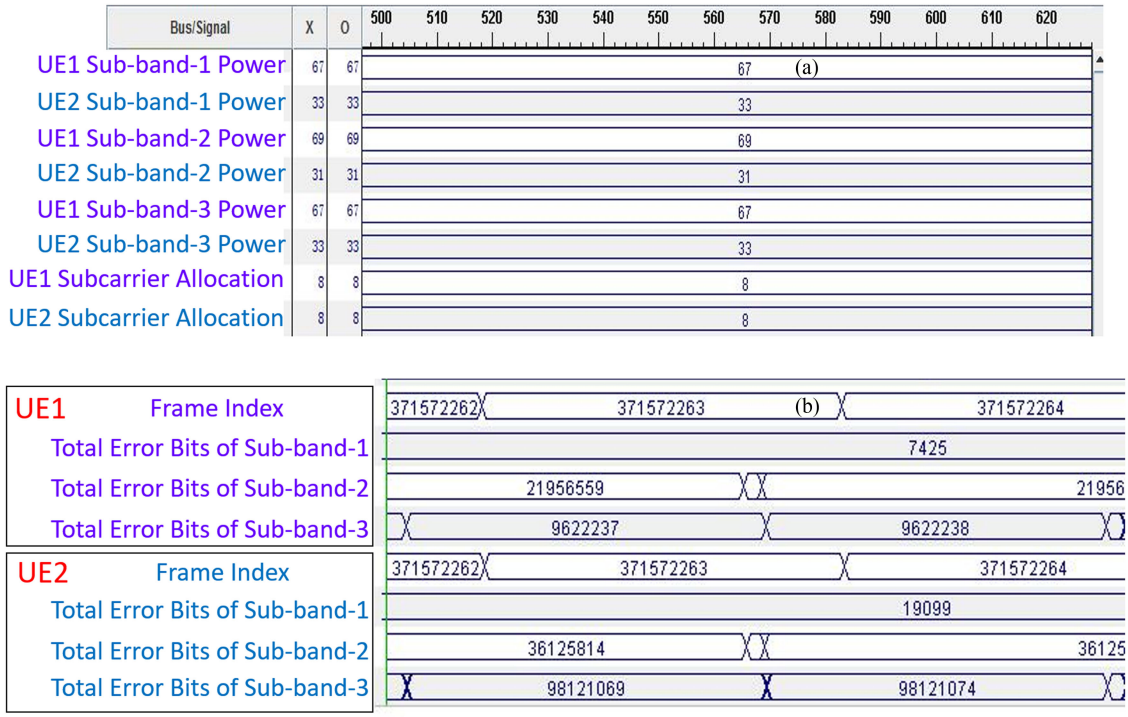

Fig. 5. (a) Real-time software-reconfigurable dynamic power-and-subcarrier input through Chipscope, and (b) real-time recorded BER measurements.

The power allocation of each sub-band for different users can be independently adjusted for performance optimization. Note that we define the total power of each subcarrier is normalized to 100. As indicated in Fig. 5(a) for sub-band-1, the power weights of UE1 and UE2 are re-assigned as 67 and 33 (which is corresponding to the power ratio of $20\log_{10}(67/33) = 6$ dB), respectively. The power can be independently adjusted in the sub-band level between UE1 and UE2, as shown in Fig. 5(a). With these power and subcarrier number settings, the transmission results of the system, including the frame index and total error bits for three sub-bands of UE1 and UE2, are shown in Fig. 5(b).

B. BER Performance With Dynamic Power Ratio Allocation for Multi-Band OFDM-NOMA

In the experiments, the power ratio is software-reconfigurable. It means that the power ratio can be dynamically adjusted in a real-time manner. Fig. 6 shows the BER distributions with respect to power ratio and received power for different sub-bands of UE1 and UE2. All data subcarriers are equally assigned to three sub-bands, i.e., sub-band-1, sub-band-2, and sub-band-3 consist of the first, middle, and last 20 data subcarriers, respectively. For the analysis of UE1, the BER performance of sub-band-1, sub-band-2, and sub-band-3 are illustrated in Fig. 6(a)–(c), respectively. As shown, the BER performance for all sub-bands gradually decreases with the increase in received power. It is because that the increased optical power results in higher signal power and thus better SNR. Moreover, when the power ratio increases, i.e., more power is allocated to UE1, the BER performance is improved accordingly since more power is assigned to UE1. Furthermore, sub-band-1 achieves best overall performance due to the good SNRs on low-frequency subcarriers. In comparison, because of the bandwidth limitation, severe frequency fading exists on high-frequency subcarriers. As a result, sub-band-3 has inferior BER performance compared to the other two sub-bands. On the other hand, Fig. 6(d)–(f) show the BER distributions for UE2 in sub-band-1, sub-band-2, and sub-band-3, respectively. Similar to UE1, increasing received power can remarkably improve the BER performance. However, for UE2, the reduction in power ratio (i.e., UE2 can obtain more power) will first decrease the BER. Then the BER of UE2 will increase if the power ratio is further decreased. This is attributed to the error propagation from UE1's decoding, as the SIC algorithm is adopted. Thus, UE2 requires an intermediate power ratio. Too large or too small power ratio will severely degrade the BER performance of UE2. In addition, similar to the results of UE1, low-frequency sub-bands of UE2 also achieve better BER performance compared to the high-frequency sub-band.

When the received optical power for UE1 and UE2 are fixed at 7 mW and 24 mW, respectively, Fig. 7(a)–(c) depicts the BERs versus received optical power for three different sub-bands, respectively. The average BER of UE1 and UE2 is considered as the metric to evaluate the overall system performance. It can be found that for the three different sub-bands, the optimal BERs are 7.4×10^{-7}, 2.0×10^{-3} and 5.5×10^{-3}, which corresponds to optimal power ratios of 9 dB, 6 dB, and 7 dB, respectively. Meanwhile, as shown in Fig. 7, with the optimal power ratios,

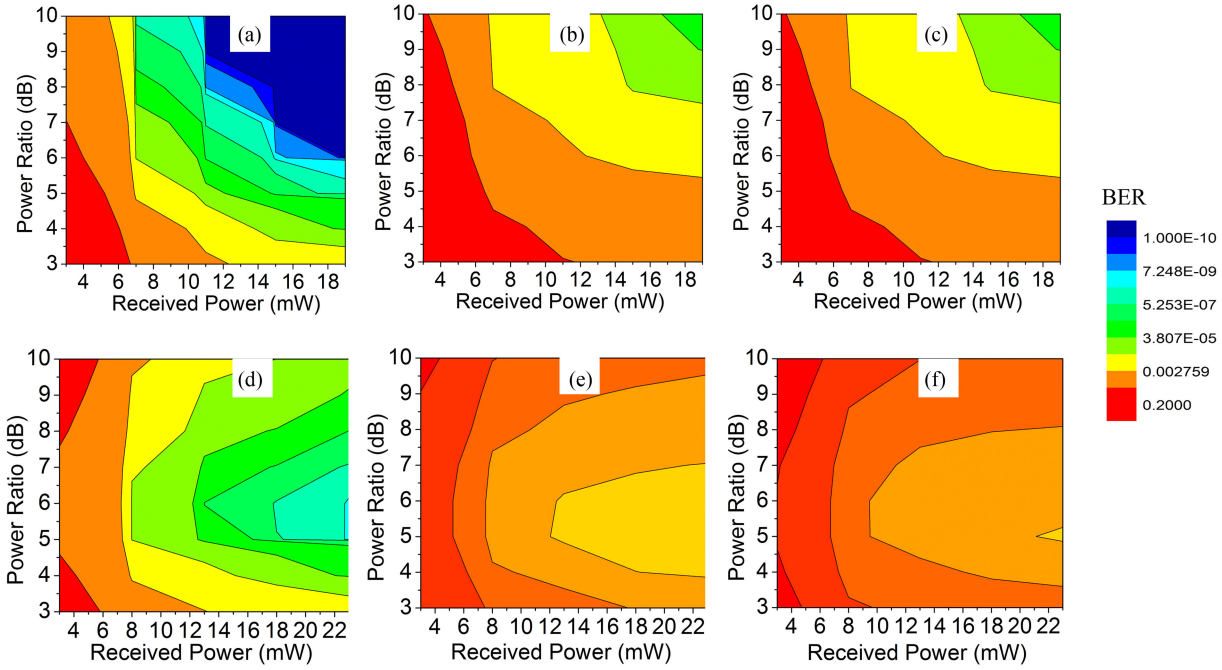

Fig. 6. BER distributions with regard to received power and power ratio for (a) UE1 sub-band-1, (b) UE1 sub-band-2, (c) UE1 sub-band-3, (d) UE2 sub-band-1, (e) UE2 sub-band-2, and (f) UE2 sub-band-3, respectively.

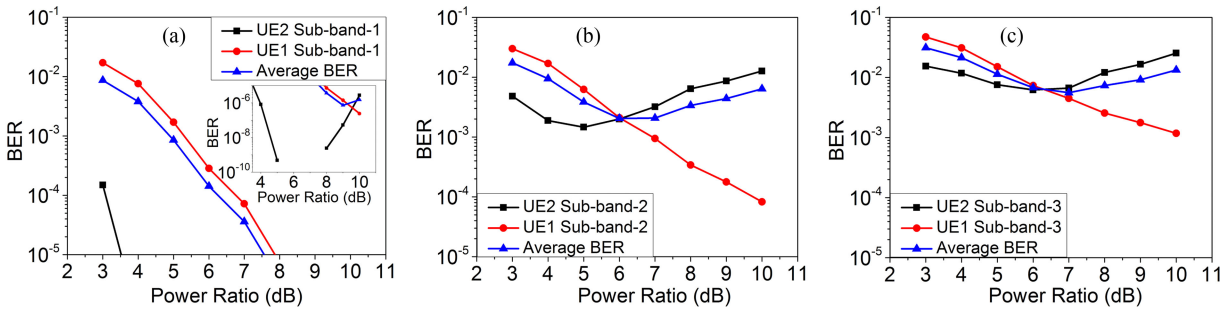

Fig. 7. BER versus power ratio for (a) sub-band-1, (b) sub-band-2, and (c) sub-band-3 at received power of 7 mW and 24 mW for UE1 and UE2, respectively. Inset in (a) depicts theperformance for additional BER range beyond that in (b) and (c).

the BERs of all sub-bands of UE1 and UE2 are nearly identical, implying that fairness among users, which is crucial for multi-user systems, is well secured by the proposed dynamic power-and-subcarrier allocation scheme.

C. Real-Time Performance Analysis With Dynamic Subcarrier Allocation

To further investigate the impact of subcarrier allocation on the OFDM-NOMA based VLC system, the data rate of UE1 is dynamically adjusted by allocating different numbers of subcarriers to UE1 under different data rates of UE2. The received power for UE1 is 7 mW and the power ratios for the three sub-bands are fixed at the optimal values of 9 dB, 6 dB, and 7 dB, as derived from Fig. 7. The corresponding BER results are shown in Fig. 8.

Fig. 8(a) shows the data rate versus the number of data subcarriers used for UE1 and UE2. Since each frame consists of two training symbols, for synchronization and channel estimation, and 100 OFDM symbols, the data rate of UE1/UE2 can be calculated by

$$Data\ Rate = \frac{M}{128} \times \frac{100}{102} \times 2\ (\text{bits/symbol}) \times 1\ \text{GSa/s} \tag{16}$$

where M is the variable number of data subcarriers, 128 is the value of the FFT size, 2 bits/symbol corresponds to the QPSK mapping for data subcarriers and 1 GSa/s is the sampling rate of the DAC. For instance, when the number of data subcarrier is set to 60, the obtained data rate is 0.92 Gbit/s ($60/128 \times 100/102 \times 2 \times 1 = 0.92$ Gbit/s). Thus, by allocating a larger number of data subcarriers to UE1/UE2, the corresponding data rate will linearly increase as well.

Generally, in real-time OFDM-NOMA system with dynamic subcarrier allocation, the BER performance of UE1 depends on

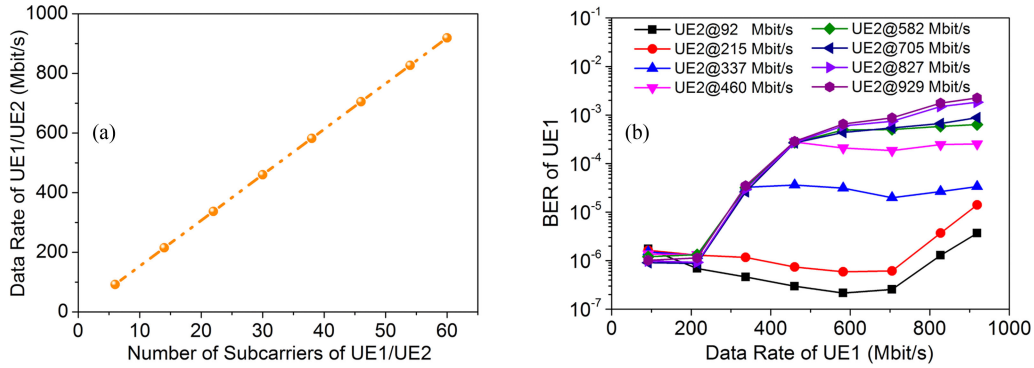

Fig. 8. (a) Data rate versus number of subcarriers for UE1 and UE2 and (b) UE1's BER versus UE1's data rate with different data rate of UE2.

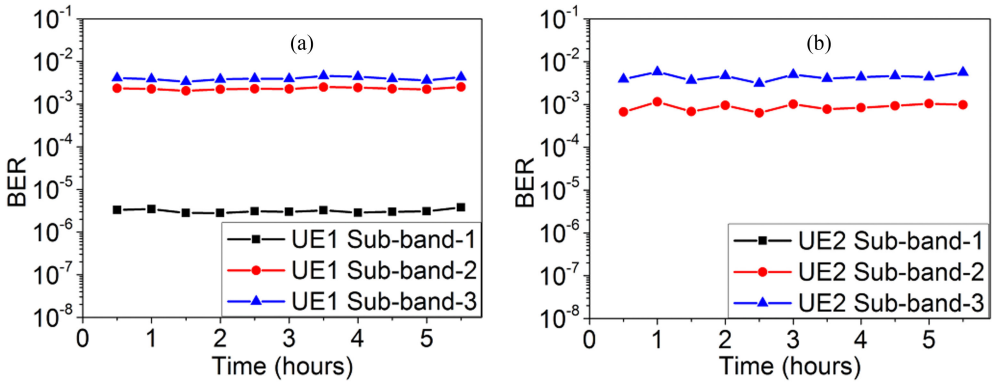

Fig. 9. System stability of real-time OFDM-NOMA system for (a) UE1 and (b) UE2 over 5.5 hours period with received optical power of 7 mW and 24 mW, respectively. Note that in the case of sub-band-1 for UE2, no error was detected during the measurements, i.e., the corresponding BERs are lower than 10^{-8} and hence are not shown in (b).

both high-frequency fading and the number of subcarrier used for UE2, as UE2's signal is seen as an overlapping interference for UE1. Fig. 8 (b) shows the BER performance versus data rate of UE1, wherein various data rates of UE2 are considered. From Fig. 8(b), firstly, we can deduce that for a fixed data rate of UE1, the BER performance of UE1 is degraded when increasing the data rate of UE2 until it is equal to the fixed data rate of UE1. It is because the noise contribution from UE2's signal to UE1's demodulation is increased accordingly since UE1 is demodulated from the overlapped signal by treating UE2 as noise. However, the BER performance of UE1 will remain nearly stable when the data rate of UE2 is further increased beyond the data rate of UE1. This is because the further increased subcarriers of UE2 do not overlap with the existing subcarriers of UE1. Fox example, when the data rate of UE1 is fixed at 337 Mbit/s, UE1 achieves BERs of 4.6×10^{-7}, 1.1×10^{-6}, 3.2×10^{-5} and 3.1×10^{-5} whilst UE2's data rate is 92, 215, 337 and 460 Mbit/s, respectively.

Secondly, it is seen in Fig. 8(b) that for a fixed data rate of UE2, the UE1's BER generally increases as its data rate increases. However, the BER performance of UE1 is relatively constant or even better when UE1'data rate is higher than that of UE2. It is because when UE1's data rate is larger than UE2's, there is no overlapping interference on some subcarriers of UE1. For example, when UE2's data rate is fixed at 460 Mbit/s, UE1 achieves BERs of 3.1×10^{-4}, 2.8×10^{-4} and 2.1×10^{-4} while UE1's data rate is 337 Mbit/s, 460 Mbit/s and 582 Mbit/s, respectively. Nevertheless, at higher data rates of UE1, UE1's BER will further increase due to the emerging high-frequency fading induced interference, as seen starting from around 705 Mbit/s in Fig. 8(b).

It is worth noting that the data-rate requirements of users can be dynamically fulfilled with the help of adjusting the user's subcarrier number in real-time. Therefore, the proposed real-time dynamic power-and-subcarrier allocation scheme is a flexible solution for practical OFDM-NOMA system to fulfill the quality of service requirements among users. Furthermore, up to 1.84 Gbit/s aggregate capacity can be realized with a BER threshold of 3.8×10^{-3} (7% FEC limit).

D. System Stability Over Time

To verify the stability of the proposed real-time OFDM-NOMA system, we have recorded the BER performance of the system over 5.5 hours. Fig. 9 shows the BERs for different sub-bands in UE1 and UE2. The received optical power for UE1 and UE2 are 7 mW and 24 mW, respectively. Meanwhile, the power ratios between UE1 and UE2 in the three sub-bands are set to 9 dB, 6 dB, and 7 dB, respectively, which are the optimal values deduced from Fig. 7. The BER results are captured every half an hour. It can be seen that all sub-bands of both users exhibit

relatively uniform BER performance over time, indicating that the whole real-time system can achieve good stability.

VI. Conclusion

We have proposed a real-time software-reconfigurable dynamic power-and-subcarrier allocation scheme for OFDM-NOMA based VLC. The flexibility and reliability of the proposed scheme are validated in a FPGA-based real-time multi-user VLC system. We incorporate both user and sub-band-level power allocation for the users to optimize the overall BER performance of the system. It is shown that at the optimal power ratios for three sub-bands, our system design can achieve nearly identical BER performance for the targeted users, ensuring the user fairness. Furthermore, we propose to use subcarrier allocation for the OFDM-NOMA system to enhance system flexibility and fulfill various capacity demands of users. The corresponding impact of the subcarrier allocation on system performance is investigated in real-time. Experimental results show that a 1.84-Gbit/s real-time OFDM-NOMA transmission can be realized with the corresponding BER below the 3.8×10^{-3} FEC limit. In addition, stable operation over long hours of the real-time system has also been demonstrated. Our proposed scheme provides a flexible, software defined platform for multi-user VLC system to ensure user fairness and fulfill diverse capacity demands.

References

[1] N. Chi, J. Shi, Y. Zhou, Y. Wang, J. Zhang, and X. Huang, "High speed LED based visible light communication for 5G wireless backhaul," in *Proc. IEEE Photon. Soc. Summer Topical Meeting Series*, 2016, pp. 4–5.

[2] D. Tsonev, S. Videv, and H. Haas, "Towards a 100 Gb/s visible light wireless access network," *Opt. Express*, vol. 23, no. 2, pp. 1627–1637, Jan. 2015.

[3] X. Lu, M. Zhao, L. Qiao, and N. Chi, "Non-linear compensation of Multi-CAP VLC system employing pre-distortion base on clustering of machine learning," in *Proc. Opt. Fiber Commun. Conf.*, 2018, Paper M2K.1.

[4] Y. Zhou, S. Liang, S. Chen, X. Huang, and N. Chi, "2.08 Gbit/s visible light communication utilizing power exponential pre-equalization," in *Proc. 25th Wireless Opt. Commun. Conf.*, 2016, pp. 1–3.

[5] Y. Hong, J. Xu, and L.-K. Chen, "Experimental investigation of multi-band OCT precoding for OFDM-based visible light communications," *Opt. Express*, vol. 25, pp. 12908–12914, 2017.

[6] X. Huang, S. Chen, Z. Wang, J. Shi, and Y. Wang, "2.0-Gb/s visible light link based on adaptive bit allocation OFDM of a single phosphorescent white LED," *IEEE Photon. J.*, vol. 7, no. 5, pp. 1–8, Oct. 2015.

[7] C.-H. Yeh, H.-Y. Chen, C.-W. Chow, and Y.-L. Liu, "Utilization of multi-band OFDM modulation to increase traffic rate of phosphor-LED wireless VLC," *Opt. Express*, vol. 23, no. 2, pp. 1133–1138, Jan. 2015.

[8] Y. Saito, Y. Kishiyama, A. Benjebbour, T. Nakamura, A. Li, and K. Higuchi, "Non-orthogonal multiple access (NOMA) for cellular future radio access," in *Proc. IEEE 77th Veh. Technol. Conf.*, 2013, pp. 1–5.

[9] F. Lu, M. Xu, L. Cheng, J. Wang, J. Zhang, and G.-K. Chang, "Non-orthogonal multiple access with successive interference cancellation in millimeter-wave radio-over-fiber systems," *J. Lightw. Technol.*, vol. 34, no. 17, pp. 4179–4186, Sep. 2016.

[10] J. A. Altabas *et al.*, "Nonorthogonal multiple access and carrierless amplitude phase modulation for flexible multiuser provisioning in 5G mobile networks," *J. Lightw. Technol.*, vol. 35, no. 24, pp. 5456–5463, Dec. 2017.

[11] Y. Tian, K.-L. Lee, C. Lim, and A. Nirmalathas, "Demonstration of non-orthogonal multiple access scheme using multilevel coding without successive interference cancellation with 60 GHz radio-over-fiber fronthaul," in *Proc. Opt. Fiber Commun. Conf.*, 2018, Paper Tu3J.4.

[12] Y. Tian, C. Lim, A. Nirmalathas, and K.-L. Lee, "Multi-cell coordination for 60 GHz RoF fronthaul enabled by a non-orthogonal multiple access scheme without successive interference cancellation," *Opt. Lett.*, vol. 43, no. 17, pp. 4236–4239, Sep. 2018.

[13] B. Lin, W. Ye, X. Tang, and Z. Ghassemlooy, "Experimental demonstration of bidirectional NOMA-OFDMA visible light communications," *Opt. Express*, vol. 25, no. 4, pp. 4348–4355, Feb. 2017.

[14] X. Guan, Q. Yang, Y. Hong, and C. C.-K. Chan, "Non-orthogonal multiple access with phase pre-distortion in visible light communication," *Opt. Express*, vol. 24, no. 22, pp. 25816–25823, Oct. 2016.

[15] J. Shi, Y. Hong, J. He, R. Deng, and L.-K. Chen, "Experimental demonstration of OQAM-OFDM based MIMO-NOMA over visible light communications," in *Proc. Opt. Fiber Commun. Conf.*, 2018, Paper M2K.3.

[16] R. Deng, J. He, Z. Zhou, J. Shi, M. Hou, and L. Chen, "Experimental demonstration of software-configurable asynchronous real-time OFDM signal transmission in a hybrid fiber-VLLC system," *IEEE Photon. J.*, vol. 9, no. 1, pp. 1–8, Feb. 2017.

[17] J. Shi, Y. Hong, R. Deng, J. He, L.-K. Chen, and G.-K. Chang, "Real-time demonstration of software reconfigurable dynamic power-and-subcarrier allocation scheme for OFDM-NOMA based multi-user visible light communications," in *Proc. Opt. Fiber Commun. Conf.*, 2019, Paper Th3I.5.

[18] S. D. Dissanayake and J. Armstrong, "Comparison of ACO-OFDM, DCO-OFDM and ADO-OFDM in IM/DD systems," *J. Lightw. Technol.*, vol. 31, no. 7, pp. 1063–1072, Apr. 2013.

[19] H. Burchardt, N. Serafimovski, D. Tsonev, S. Videv, and H. Haas, "VLC: Beyond point-to-point communication," *IEEE Commun. Mag.*, vol. 52, no. 7, pp. 98–105, Jul. 2014.

[20] J. Xiao *et al.*, "Hadamard transform combined with companding transform technique for PAPR reduction in an optical direct-detection OFDM system," *IEEE/OSA J. Opt. Commun. Netw.*, vol. 4, no. 10, pp. 709–714, Oct. 2012.

[21] H. Chen, J. He, J. Tang, F. Li, M. Chen, and L. Chen, "Performance of 16 QAM-OFDM with new null subcarrier shifting in an intensity-modulated direct detection system," *IEEE/OSA J. Opt. Commun. Netw.*, vol. 6, no. 2, pp. 159–164, Feb. 2014.

[22] J. Armstrong, "OFDM for optical communications," *J. Lightw. Technol.*, vol. 27, no. 3, pp. 189–204, Feb. 2009.

[23] S. M. R. Islam, N. Avazov, O. A. Dobre, and K. S. Kwak, "Power-domain non-orthogonal multiple access (NOMA) in 5G systems: Potentials and challenges," *IEEE Commun. Surveys Tuts.*, vol. 19, no. 2, pp. 721–742, Second quarter 2017.

[24] M. Chen, J. He, Q. Fan, Z. Dong, and L. Chen, "Experimental demonstration of real-time high-level QAM-encoded direct-detection optical OFDM systems," *J. Lightw. Technol.*, vol. 33, no. 22, pp. 4632–4639, Nov. 2015.

[25] M. Chen, J. He, and L. Chen, "Real-time optical OFDM long-reach PON system over 100 km SSMF using a directly modulated DFB laser," *IEEE/OSA J. Opt. Commun. Netw.*, vol. 6, no. 1, pp. 18–25, Jan. 2014.

[26] R. Deng, J. He, M. Chen, Y. Wei, J. Shi, and L. Chen, "Real-time VLLC-OFDM HD-SDI video transmission system with TS-based SFO estimation," in *Proc. Opt. Fiber Commun. Conf. Exhib.*, 2017, Paper M1K.6.